

GLOBAL CLIMATE AND ATMOSPHERE COMPOSITION OF THE ULTRA-HOT JUPITER WASP-103b FROM *HST* AND SPITZER PHASE CURVE OBSERVATIONS

LAURA KREIDBERG,^{1,2} VIVIEN PARMENTIER,³ MICHAEL R. LINE,⁴ KEVIN B. STEVENSON,⁵ TOM LOUDEN,⁶
MICKÄEL BONNEFOY,⁷ JACQUELINE K. FAHERTY,⁸ GREGORY L. HENRY,⁹ KEIVAN STASSUN,¹⁰ JACOB L. BEAN,¹¹
JONATHAN FORTNEY,¹² ADAM SHOWMAN,³ AND JEAN-MICHEL DÉSSERT¹³

¹*Harvard Society of Fellows 78 Mt. Auburn St.*

Cambridge, MA 02138, USA

²*Harvard-Smithsonian Center for Astrophysics 60 Garden St.*

Cambridge, MA 02138

³*Department of Planetary Sciences and Lunar and Planetary Laboratory, The University of Arizona*

⁴*Arizona State University*

⁵*Space Telescope Science Institute*

⁶*University of Warwick*

⁷*Université Grenoble Alpes*

⁸*American Museum of Natural History*

⁹*Center of Excellence in Information Systems, Tennessee State University*

¹⁰*Vanderbilt University*

¹¹*University of Chicago*

¹²*University of California Santa Cruz*

¹³*University of Amsterdam*

Submitted to ApJ

ABSTRACT

We present thermal phase curve measurements for the hot Jupiter WASP-103b observed with *Hubble*/Wide Field Camera 3 and *Spitzer*/IRAC. The dayside planet-to-star flux ranges from FIXME to FIXME at $1.1 - 4.5 \mu\text{m}$. The phase curves are symmetric and large amplitude, indicative of poor redistribution. We fit the phase curves with the SPIDERMAN package to determine the brightness distribution in the photosphere, and find the peak dayside temperature ranges from FIXME to FIXME depending on model. We also generate phase-resolved spectra, which are consistent with blackbody models for the planet's emission at near-infrared wavelengths, but show strong emission features in the *Spitzer* bands. We attribute these features to CO emission and a thermal inversion. The retrieved atmospheric composition is more metal-enriched than other hot Jupiters (FIXME). The carbon-to-oxygen ratio is consistent with solar composition. The absence of water features is due to BLAH. We compare the phase curves to general circulation models and find that atmospheric drag is required. We also compare the spectra to brown dwarfs and young directly imaged companions and find that the water features are significantly diminished in amplitude. power of phase curve observations to elucidate the three-dimensional structure of exoplanet atmospheres.

inversion on the dayside but not on the nightside

Keywords: planets and satellites: individual (WASP-107b), planets and satellites: atmospheres

1. INTRODUCTION

Planets are round, rotating, and irradiated on one hemisphere at a time – all of which contribute to rich spatial structure in their climate and atmospheric composition. Short period, tidally locked planets are an extreme example, with hot, continuously illuminated day-sides. This asymmetry is expected to produce large gradients in temperature, chemistry, and cloud coverage with longitude (Showman et al. 2009; Kataria et al. 2016; Parmentier et al. 2016), and provides an opportunity to learn about atmospheric dynamics in a very different regime from the Solar System planets.

Exoplanets are so distant that they are not spatially resolved, so the only way to reveal inhomogeneity in their atmospheres is to measure a phase curve. Phase curve observations consist of continuous monitoring of the planet-to-star flux ratio over a complete orbital revolution of the planet, which exposes different longitudes at each orbital phase. The first phase curve was observed with *Spitzer* for the hot Jupiter HD 189733b by (Knutson et al. 2007), followed by additional *Spitzer* observations for about a dozen more systems (cataloged in Parmentier & Crossfield 2017). The observations revealed large day-night temperature contrasts (in excess of 300 K), and eastward shifted peak brightness due to heat circulation, as predicted by 3D models (Showman et al. 2009). These infrared measurements were complemented by optical phase curves from *Kepler* which show evidence for reflected light from patchy and variable day-side clouds with a range of compositions (Demory et al. 2013; Hu et al. 2015; Armstrong et al. 2016; Parmentier et al. 2016). A *spectroscopic* phase curve was observed for WASP-43b with *Hubble*/Wide Field Camera 3 (*HST*/WFC3) in the near-infrared, which provided the first phase-resolved measurements of an exoplanet’s water abundance and thermal structure (Stevenson et al. 2014b, 2017).

In this paper we present spectroscopic phase curve observations of the hot Jupiter WASP-103b, measured with *HST*/WFC3 and *Spitzer*/IRAC. This planet is an ideal target for phase curve observations, with an orbital period of just 22 hours and an equilibrium temperature of 2500 K (Gillon et al. 2014). Previous observations of WASP-103b’s atmosphere revealed a blackbody-like dayside emission spectrum, with possible evidence for a K_S -band emission feature (Cartier et al. 2017; Delrez et al. 2018). The optical transmission spectrum shows evidence for strong sodium and potassium absorption features that are consistent with expectations for a cloud-free atmosphere (Lendl et al. 2017).

WASP-103b is an archetype of the class of ultra-hot Jupiters (with orbital periods of about one day and day-

side temperatures typically > 2000 K). Observations of the thermal emission spectra of these objects have been puzzling. In the near-infrared, where water is the dominant absorber, some spectra show water absorption features, some show emission features, and some are consistent with blackbody models (Madhusudhan et al. 2011; Crossfield et al. 2012; Stevenson et al. 2014a; Haynes et al. 2015; Evans et al. 2016; Beatty et al. 2017a,b; Sheppard et al. 2017; Arcangeli et al. submitted; Mansfield et al. submitted). A variety of explanations have been proposed for these results, including low metallicity or high carbon-to-oxygen compositions, dayside clouds, and isothermal or inverted temperature profiles caused by TiO/VO absorption in the upper atmosphere. Recently, Arcangeli et al. (submitted) showed that water dissociation on the hot dayside plays an important role in the atmospheres of these ultra-hot planets and may be responsible for some of the blackbody-like near-IR spectra. In this work, we put these results in context investigate the global thermal structure of WASP-103b over a range of temperatures. **FIXME**

The structure of the paper is the following: in §2 we describe the observations and data reduction. §3 details the models fit to the phase curves. §4 we discuss results, including the phase-resolved spectra, a comparison of thermal phase variation models, and **FIXME**. In §6 and 7, we compare the observations to GCM predictions and spectra from similar temperature stars and directly imaged companions. §8 concludes.

2. OBSERVATIONS AND DATA REDUCTION

We observed two full-orbit phase curves of WASP-103b with *HST*/WFC3 and one each with *Spitzer*/IRAC at 3.6 and 4.5 μm (from *HST* Program 14050 and *Spitzer* Program 11099). We also reduced two *HST*/WFC3 secondary eclipse observations of WASP-103b from *HST* Program 13660 (PI: M. Zhao).

2.1. *HST*/WFC3

The *HST* phase curve observations consisted of two visits on 26-27 February and 2-3 August 2015. Each visit was 15 orbits in duration and spanned 23 hours. The last half of orbit 15 in each visit was used for a gyro bias update and does not produce useable science data. We took a direct image of the star with the F126N filter at the beginning of each orbit to determine the wavelength solution zero-point. The remainder of the orbit consisted of time-series spectroscopy with the G141 grism (1.1 – 1.7 μm) and the 256 x 256 pixel subarray. We used the SPARS10/NSAMP = 15 read-out mode, which has an exposure time of 103 seconds. To optimize the duty cycle of the observations, we used the spatial

scan observing mode with a scan rate of 0.03 arcsec/s, alternating between forward and backward scanning on the detector. The scan height was 25 pixels and the peak counts were 35×10^3 photoelectrons per pixel. We collected a total of 18 spatial scan exposures per orbit. The two eclipse observations from Program 13660 had a similar observing setup (described in detail in [Cartier et al. 2017](#)).

We reduced the data from both programs using a custom pipeline developed for past analyses of WFC3 data (for details see [Kreidberg et al. 2014a,b, 2015](#)). Briefly, we use the optimal extraction algorithm of [Horne \(1986\)](#) to extract each up-the-ramp sample (or “stripe”) separately. The stripes are then summed to create the final spectrum. For each stripe, the extraction window is 24 pixels high and centered on the stripe midpoint. We estimate the background from the median of a region of the detector that is uncontaminated by the target spectrum (rows 5-50). The typical background counts are low (10-15 photoelectrons per pixel, roughly 0.03% of the peak counts from the target star). We note that the extracted spectrum includes flux from a nearby companion star, which is separated from WASP-103 by less than two pixels (0.2”; [Wöllert & Brandner 2015](#)). Our extracted spectrum includes flux from this star, which we account for later in the analysis.

2.2. *Spitzer*

We also obtained *Spitzer*/IRAC observations with 3.6 and 4.5 μm photometric filters (referred to as Channel 1 and Channel 2, respectively). The observations had the following setup. Each phase curve observation consisted of 30 hours of time series photometry, beginning three hours prior to one secondary eclipse and ending three hours after a second eclipse. We used 12 s exposures to maximize the duty cycle without saturating the detector. The data volume is relatively low for this exposure time, so we read out the full array. To minimize the intrapixel effect (variations in flux caused by imprecise pointing), we did not dither and also used PCRS peak-up¹ to improve the pointing accuracy. We began each observations with a 30-minute position settling period, followed by three Astronomical Observation Requests (AORs) of equal duration. At the beginning of each AOR, the telescope was repointed to position the target in the “sweet spot” of the detector.

The data were reduced with the POET pipeline ([Stevenson et al. 2012](#)). We performed aperture photometry with an aperture size of 2.75 pixels (chosen from

a grid of apertures between 2 and 4 pixels to minimize the residual noise in the light curve fits). We masked pixels that were flagged in the bad pixel mask provided in the ancillary data for the observations. The target centroid was determined with a two-dimensional Gaussian fit. We estimated and subtracted the background from an annulus with a radius of 7 to 15 pixels from the centroid. As for the *HST* observations, the contaminating flux from the nearby star is included in the final photometry and corrected later in the light curve fits.

2.3. *Photometric Monitoring*

We monitored WASP-103’s photometric variability over 158 nights during 2014 - 2016 with the Tennessee State University Celestron 14-inch (C14) automated imaging telescope (AIT), located at Fairborn Observatory in southern Arizona ([Henry 1999](#)). The observations of WASP-103 were made in the Cousins R pass-band with an SBIG STL-1001E CCD camera. Each observation consisted of 4–10 consecutive exposures on WASP-103 along with several dozen comparison stars in the same field. The individual consecutive frames were co-added and reduced to differential magnitudes (i.e., WASP-103 minus the mean brightness of the six best comparison stars). The nightly observations were corrected for bias, flat-fielding, pier-side offset, and differential atmospheric extinction.

The photometric analyses are summarized for each observing season in Table 1. The standard deviation of WASP-103’s brightness in each season is given in column 4. The mean of the three standard deviations is 0.0058 mag, which is very comparable to the mean standard deviation of the six comparison stars (0.0055 mag). To maximize the possibility of detection WASP-103’s rotation, we normalized the photometry such that each observing season has the same mean, thereby removing long-term variability in WASP-103 and/or the comparison stars. We performed a periodogram analysis of the normalized dataset. Figure 1 shows the frequency spectrum and the phase curve computed with the best frequency, respectively. We also performed a least-squares fit to the data to determine the best fit sine curve. The best fit period is 6.814 days, which agrees closely with the estimated stellar rotation period of 6.855 days ([Gillon et al. 2014](#)). The variability amplitude is 0.005 mag. Based on the formalism in [Zellem et al. \(2017\)](#), we calculate that this variability will bias the measured eclipse depth by $\lesssim 10$ ppm from epoch to epoch, which is well below the photon-limited precision of our measurements.

3. LIGHT CURVE FITS

¹ http://irsa.ipac.caltech.edu/data/SPITZER/docs/irac/pcrs_obs.shtml

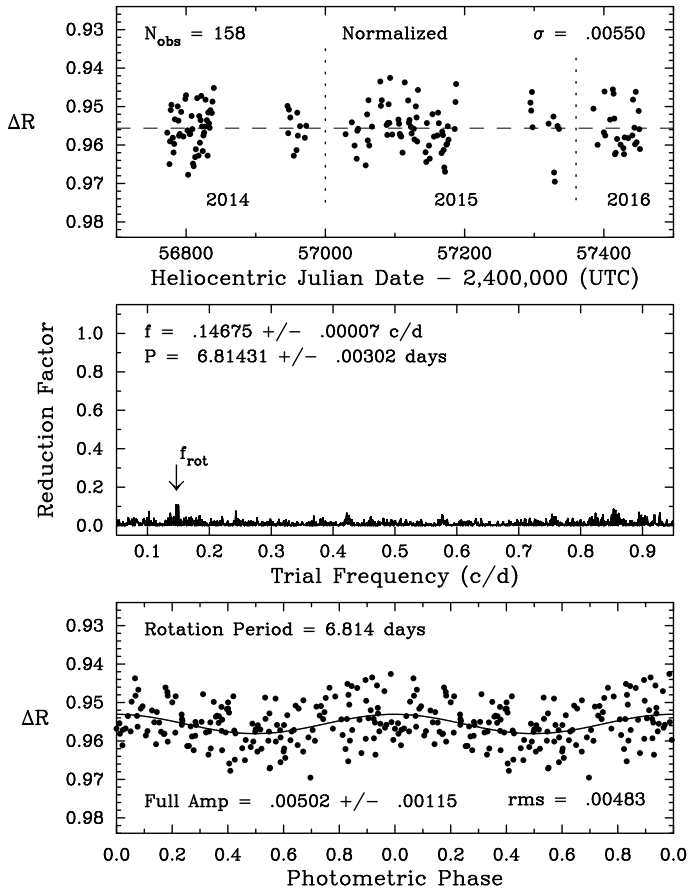


Figure 1. *Top:* The normalized nightly Cousins R band photometric dataset for WASP-103, acquired with the C14 automated imaging telescope at Fairborn Observatory. Vertical dashed lines denote separate observing seasons. Gaps are due to target visibility and the Arizona monsoon season (July - September). *Middle:* The frequency spectrum of the normalized dataset suggests low-amplitude variability with a period of 6.814 days. *Bottom:* The normalized dataset phased to the 6.814-day period, which we interpret as the stellar rotation period. A least-squares sine fit to the 6.814-day rotation period gives a peak-to-peak amplitude of just 0.005 mag.

Table 1. Photometric Observations of WASP-103

Observing	Date Range	Sigma	Seasonal Mean
2014	59 56722–56972	0.0057	0.9546 ± 0.0007
2015	73 57028–57335	0.0062	0.9549 ± 0.0007
2016	26 57385–57451	0.0055	0.9485 ± 0.0011

We fit a two-component model to the light curves. One component models the astrophysical signal (the planet’s thermal phase variation and transit), and the other component models the systematic noise introduced by time-dependent changes in instrument performance. For each light curve, we fit the physical and systematic components simultaneously, such that the total observed flux as a function of time is given by $F(t) = F_{\text{physical}}(t) \times F_{\text{sys}}(t)$. For the *HST* data, where we observed two phase curves and two additional eclipses, we constrain the physical parameters to be the same for all visits, but allow some of the systematics parameters to vary (for more details see § 3.2.1). We fit the WFC3 band-integrated (“white” light curve), as well as spectroscopic light curves created from 10 wavelength bins uniformly spaced at $0.05 \mu\text{m}$ intervals between 1.15 and $1.65 \mu\text{m}$.

3.1. Astrophysical Signal

We assume the measured astrophysical signal F_{physical} has the following form:

$$F_{\text{physical}}(\lambda, t) = T(\lambda, t) + c(\lambda, t) \times F_p/F_s(\lambda, t) \quad (1)$$

where $T(\lambda, t)$ is the transit model (the fraction of the stellar disk that is visible at time t), $F_p/F_s(\lambda, t)$ is the disk-integrated planet-to-star flux, and c is a correction factor for companion star dilution and the planet’s tidal distortion.

We calculated the transit model $T(t)$ with the *batman* package (Kreidberg 2015). Many of the physical parameters are tightly constrained by Southworth et al. (2015), so we fixed the orbital period, time of inferior conjunction, orbital inclination, and ratio of semi-major axis to stellar radius to the previously published values ($P = 0.925545613$ day, $t_0 = 2456836.2964455$ BJD_{TDB}, $i = 87.3^\circ$, and $a/R_s = 2.999$). As a test, we fit for these parameters with the *Spitzer* Channel 2 light curve, which has the best phase coverage and least systematic noise of the three data sets. We found that the transit parameters are consistent with the Southworth et al. (2015) results, so we proceeded with the remainder of the analysis holding those parameters fixed. The free parameters for the transit model were the transit depth r_p and a linear limb darkening parameter u .

We calculated the planet-to-star flux F_p/F_s in two different ways. First, we fit a sinusoid with a period equal to the planet’s orbital period. The free parameters were the sine curve amplitude and phase offset. For the second approach, we used the *SPIDERMAN* package (Louden & Kreidberg 2017) to model F_p/F_s . This package allows users to input a climate map (temperature or brightness as a function of latitude and longitude),

and generate the corresponding flux ratio for an observation at time t . In our fit, we calculated the stellar flux with a PHOENIX model (Husser et al. 2013) interpolated to an effective temperature of 6110 K (Gillon et al. 2014). For the planet flux, we tested three different maps: a two-temperature map, with a uniform dayside temperature T_d and a uniform nightside temperature T_n ; a map generated with spherical harmonics; and the physically-motivated kinematic model from Zhang & Showman (2017), which has just three free parameters (the nightside temperature T_n , the change in temperature from day-to-night side Δ_T , and the ratio of radiative to advective timescales ξ). In all cases, we assumed that the planet is tidally locked, such that each orbital revolution corresponds to one complete rotation on its spin axis.

We scaled the planet-to-star flux by a correction factor c to account for dilution from the companion star and ellipsoidal variability due to the planet’s tidal distortion. The correction factor took the form:

$$c(\lambda, t) = [1 + \alpha(\lambda)]A(t) \quad (2)$$

where $\alpha(\lambda)$ is the additional fractional flux from the companion star and $A(t)$ is the sky-projected area of the planet. We estimated $\alpha(\lambda)$ based on the best fit spectral energy distribution from Cartier et al. (2017). The companion star contribution ranges from 10% at $1.1 \mu\text{m}$ to 16% at $4.5 \mu\text{m}$. The uncertainty on the companion star flux contribution is less than 1%, which introduces negligible error in the estimated planet-to-star-flux compared to the photon noise. We calculated $A(t)$ using the analytic formula from Leconte et al. (2011a), equation B.9, which computes the projected area of a triaxial ellipsoid. We estimated the ellipsoid properties using Table B.3 of Leconte et al. (2011b), assuming the planet radius is $1.5 R_{\text{Jup}}$ and age is 5 Gyr. The predicted ellipsoidal variability is shown in Figure 2. At quadrature, the projected radius is 8% larger than at phase zero (mid-transit). We also considered the effects of Doppler beaming and found that it contributes less than 10 ppm variability to the measured flux (Loeb & Gaudi 2003).

3.2. Systematics

Both the *HST* and *Spitzer* phase curves have systematic noise caused by variations in the sensitivity of the instrument over time. For the *HST*/WFC3 data, the dominant systematic is an orbit-long exponential trend due to charge traps filling up over successive exposures (Long et al. 2015; Zhou et al. 2017). For *Spitzer* the primary source of noise is the intrapixel sensitivity effect. The detector’s pixels do not have uniform sensitivity, so slight changes in telescope pointing cause the recorded

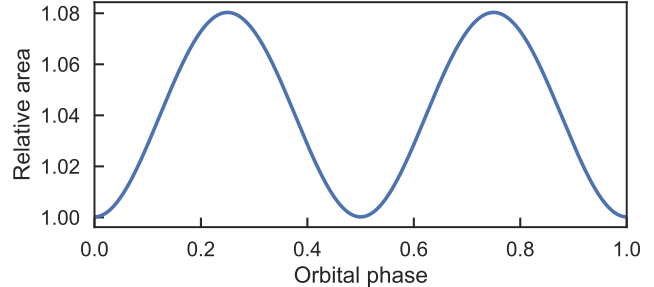


Figure 2. Projected area of the planet as a function of orbital phase, normalized to unity at phase zero. The area variation was predicted analytically using the model from Leconte et al. (2011a).

flux to vary. In Figure 3, we show the raw light curves before systematic noise was removed. The systematics have comparable amplitude to the thermal phase variation signal, so they must be carefully corrected to recover the underlying planet-to-star flux.

3.2.1. *HST* Systematics

We fit the WFC3 systematics using an analytic model of the form:

$$F_{\text{sys}}(t) = (c S(t) + v_1 t_v + v_2 t_v^2)(1 - \exp(-a t_{\text{orb}} - b)) \quad (3)$$

where t_v is time elapsed since the first exposure in a visit and t_{orb} is time since the first exposure in an orbit. $S(t)$ is a scale factor equal to 1 for exposures with spatial scanning in the forward direction and s for reverse scans, to account for the upstream-downstream effect (McCullough & MacKenty 2012). The orbit-long ramp parameters are consistent for all the visits, so we constrained a , b , and s to have the same value for all visits in the final fit. The visit-long trends differ from visit to visit, so c , v_1 , and v_2 were allowed to vary between visits. We fixed v_2 to zero for the two secondary eclipse observations from Program 13360, since the visit-long trend for shorter observations is fit well by a linear slope.

Some segments of the data exhibit stronger systematics than others, so we exclude these data in our final analysis. We drop the first orbit from every visit and the first exposure from every orbit (following common practice; see e.g. Kreidberg et al. 2014a). We also discard exposures from the last half of orbit 15 from the phase curve observations, which were taken in staring mode to enable a gyro bias update. Since we observed two phase curves, we have complete orbital phase coverage the planet despite discarding some data.

3.2.2. *Spitzer* Systematics

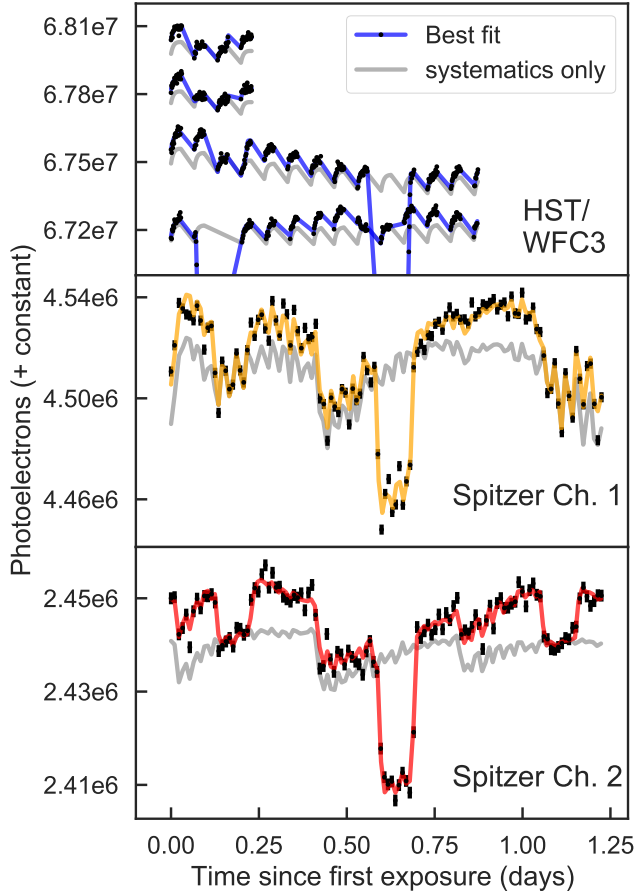


Figure 3. Raw light curves for WASP-103b observed with *HST*/WFC3 (top panel) and *Spitzer*/IRAC (bottom two panels). The data points are indicated with black dots. The *HST* data are unbinned, and the *Spitzer* data are binned in time segments of 15 minutes with error bars indicating the bin standard deviation. The colored lines show the best fit models, which include the astrophysical signal and instrument systematics. The gray lines indicate the contribution from the instrument systematics alone (which would be observed for a source with constant brightness and no planet). For visual clarity, we corrected the *HST* data for the upstream-downstream effect, separated the four visits by adding a flux offset, and zoomed in on the phase variation, so the transits are not displayed in the panel.

We fit the *Spitzer* systematics with the POET pipeline, which uses the BLISS mapping technique (Stevenson et al. 2012). This approach creates a map of the intrapixel sensitivity while simultaneously fitting for other systematics and the physical parameters of the system. The sensitivity map is determined by bilinear interpolation over a grid of knots centered on the stellar flux. Each knot’s sensitivity is calculated from the residuals to the light curve fit: the higher the flux values

for data points near a given knot, the higher the detector sensitivity is at that position. To avoid overfitting, we chose the grid scale such that bilinear interpolation performed better than nearest neighbor interpolation. For the $3.6\,\mu\text{m}$ data, the grid scale was 0.008 pixel in both x and y . For $4.5\,\mu\text{m}$, the scale was 0.022 pixel. In addition to the intrapixel sensitivity variation, we fit the data for a linear trend in time. We tested a quadratic trend but did not find significant evidence for the additional model complexity based on the Bayesian information criterion (BIC).

3.3. Best Fits and Uncertainties

To determine the best fits, we performed a least-squares χ^2 minimization for each wavelength and model. For a subset of these cases, we also performed a Markov chain Monte Carlo (MCMC) analysis to estimate parameter uncertainties. We used *emcee* (Foreman-Mackey et al. 2013) to fit the *HST*/WFC3 light curves and differential evolution Monte Carlo for the *Spitzer* fits (Braak 2006). We ran the MCMC until convergence according to the Gelman-Rubin statistic *FIXME*. MCMC techniques only produce robust uncertainties when the noise is normally distributed and white, so to account for correlated noise in the $3.6\,\mu\text{m}$ light curve (described in §3.4) we fit the wavelet model from Carter & Winn (2009) (simultaneously with the other model parameters). We used a Haar wavelet and let the power spectral density of the red noise vary, following Diamond-Lowe et al. (2014). In our final fit, the noise power spectrum $1/f^\gamma$ had $\gamma = 1.1 \pm 0.1$.

3.4. Goodness of Fit

We performed several tests of the quality of the light curve fits. First we predicted the level of scatter in the light curves based on photon noise alone, then compared this value to the root-mean-square (rms) of the fit residuals. The *Spitzer* $4.5\,\mu\text{m}$ light curve rms is within 10% of the expected photon noise limit (691 versus 640 ppm), whereas the $3.6\,\mu\text{m}$ light curve has significantly larger rms (797 versus 470 ppm), due to time-correlated red noise (discussed below). The expected photon-limited rms for the WFC3 spectroscopic light curves ranges from 430 - 530 parts per million (ppm), and the measured rms was typically within 5% of expectations for all spectroscopic channels. For the WFC3 band-integrated white light curve, the rms was slightly larger than predicted (175 versus 122 ppm). There are a number of possible origins for this discrepancy, including imperfect background subtraction, variation in the position of the spatial scan on the detector, loss of flux outside the extraction window, and imperfect modeling of the astrophysical signal or instrument systematics. However,

our analysis of the composition and thermal structure of the planet’s atmosphere is based on the wavelength-dependent data (where we reach the photon limit), so we do not further explore the small excess noise in the white light curve.

In addition to calculated the fit rms compared to the photon noise, we also tested for the presence of red noise based on whether the rms decreases as expected when the light curve is binned in time. If the noise is white (uncorrelated in time), the residuals are expected to decrease by a factor of \sqrt{N} , where N is the number of points in a bin. Figure 4 shows the binned residuals compared to expectations for white noise. The *HST*/WFC3 and *Spitzer* Channel 2 light curves agree well with expectations, whereas *Spitzer* Channel 1 shows higher noise than expected as bin size increases. This test confirms the presence of time-correlated noise in the Channel 1 light curve that can be seen by eye in the residuals in Figure 5. Both *Spitzer* channels use the same detector, but Channel 1 data are more susceptible to time-correlated noise because the the point spread function is narrower at shorter wavelengths, making intrapixel sensitivity variations more pronounced.

4. RESULTS

The fitted light curves are shown in Figure 5. This figure shows results from the spherical harmonics model for the thermal phase variation and has instrument systematics removed. Broadly speaking, the phase curves show large amplitude phase variation, ranging from 1.5 parts-per-thousand (ppt) in the WFC3 bandpass to 5 ppt in *Spitzer* Channel 2. The planet flux changes significantly with orbital phase in all three of the data sets, suggesting a strong gradient from dayside to nightside temperature, and peak brightness occurs near phase 0.5. In this section, we quantitatively characterize the phase curve shape, split the data into phase resolved spectra, evaluate different different temperature maps, and compare with previous observations of the dayside thermal emission spectrum.

4.1. Phase Curve Amplitudes and Hotspot Offsets

The shape of a phase curve can be summarized with two parameters: the amplitude of thermal phase variation (minimum to maximum brightness, divided by the secondary eclipse depth) and the location of peak brightness (typically called a “hotspot offset” and measured in degrees eastward of the substellar point). Table 2 lists the estimated amplitudes and hotspot offsets (median and 1σ credible interval) for the band-integrated WFC3 phase curve and both *Spitzer* channels. The estimates are from the sine curve model for the thermal phase variation, which fits directly for the amplitude and offset.

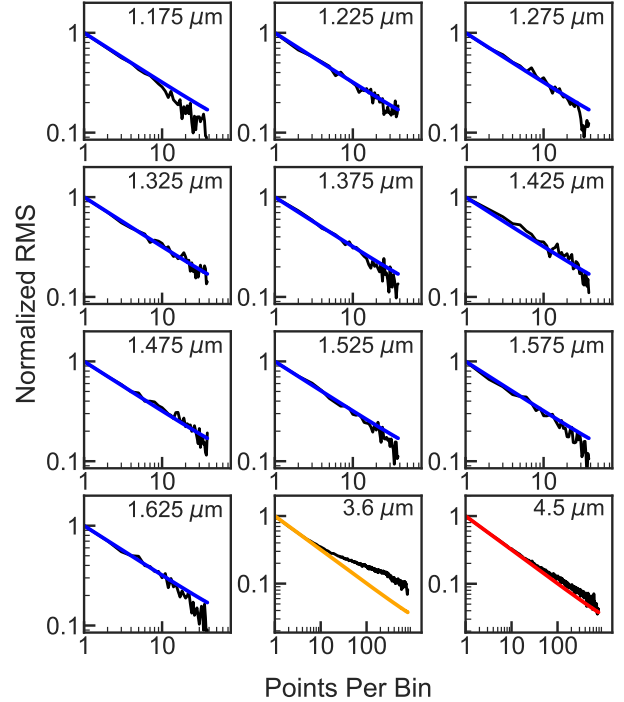


Figure 4. Root mean square (rms) variability in the light curves as a function of bin size (black lines) compared to the expected rms from photon noise (colored lines). The central wavelength of the light curve is indicated in the upper right corner of each panel. With the exception of the *Spitzer* 3.6 μm channel, the rms for the light curves bins down in agreement with predictions from the photon noise.

For all three phase curves, the hotspot offset is consistent with zero degrees, indicative of a fast radiative-to-advective timescale (the incident flux is reradiated to space faster than it is advected around to the nightside). Fast radiative timescales are predicted at high temperatures, and small hotspot offsets are also observed for other very hot Jupiters (Komacek et al. 2017). The phase curve amplitudes are large (near 0.8 - 0.9), as expected for an atmosphere with inefficient heat redistribution. In § 6 we compare these results to expectations from 3D GCMs.

4.2. Phase-Resolved Spectra

We used the best-fit phase curves (with systematics removed) to generate phase-resolved emission spectra. Since our model does not fit eclipse depth as a free parameter, we estimated the dayside emission spectrum as follows. We used SPIDERMAN’s eclipse_depth method to calculate the average planet-to-star flux for the best-fit model during secondary eclipse. To estimate uncer-

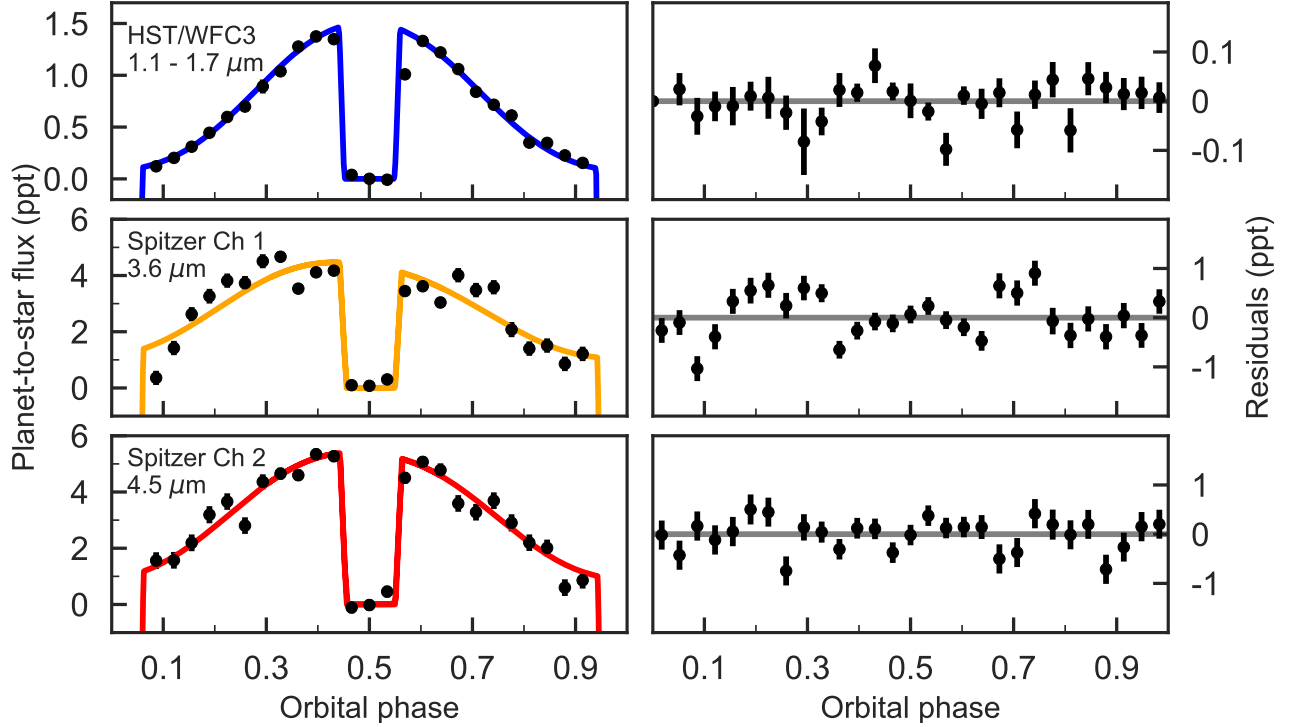


Figure 5. WASP-103b phase curve observations from *HST*/WFC3 (top) and *Spitzer*/IRAC (middle and bottom). For clarity, the data are phase-folded on the planet’s orbital period and binned in 30 uniformly spaced bins between 0 and 1. The left column shows the phase curves with systematic noise removed (black points) compared to the best fit spherical harmonics model (colored lines). The error bars denote 1σ uncertainties (in some cases, the errors are smaller than the data points). We include the transits in the fit, but they are not displayed in this figure. The right-hand column shows the binned residuals for the best-fit light curve.

tainties, we took the standard deviation of the residuals of the in-eclipse data points, then added this value in quadrature to the standard deviation of the residuals of the out-of-eclipse data. This quadrature sum accounts for the uncertainty in the baseline flux. To account for red noise in the *Spitzer* 3.6μ light curve, we use the approach of Pont et al. (2006) to determine the red noise contribution on the timescale of the eclipse. We add the estimated red noise in quadrature, which increases the uncertainty on planet-to-star flux by a factor of 2.5.

For the other orbital phases, we binned the light curve (with systematics removed) in eight intervals of about 0.1 in orbital phase, with endpoints at phases 0.06, 0.15, 0.25, 0.35, 0.44 and 0.56, 0.65, 0.75, 0.85, 0.94. These endpoints were chosen to ensure that there is no contribution from in-transit or in-eclipse data. In each phase bin, we estimated the planet-to-star flux from the mean value of the data points in the bin. To estimate the uncertainty, we took the standard deviation of the points in the bin and added it in quadrature to the standard deviation of the data points during secondary eclipse

(phase 0.46 – 0.54), to account for the uncertainty in baseline stellar flux. For the 3.6μ data, we also add red noise on the timescale of a phase bin, following Pont et al. (2006). The phase-resolved emission spectra are shown in Figure 7 and listed in Table 3.

To test that the phase-resolved spectra are robust to different approaches for fitting the data, we compared the spectra for all four of the thermal phase variation models (sinusoid, kinematic, spherical harmonics, and two temperature). We found that the choice of model does not significantly change the results. The emission spectra are insensitive to the models because they are estimated directly from the data (after systematics have been removed). Since systematic noise is not strongly correlated with the astrophysical signal, the systematics-divided data are nearly identical for all the models. This point is illustrated in Figure 6 for the broadband WFC3 light curve. In most phase bins, the planet-to-star flux agrees to well within one sigma for all the models.

4.3. Climate

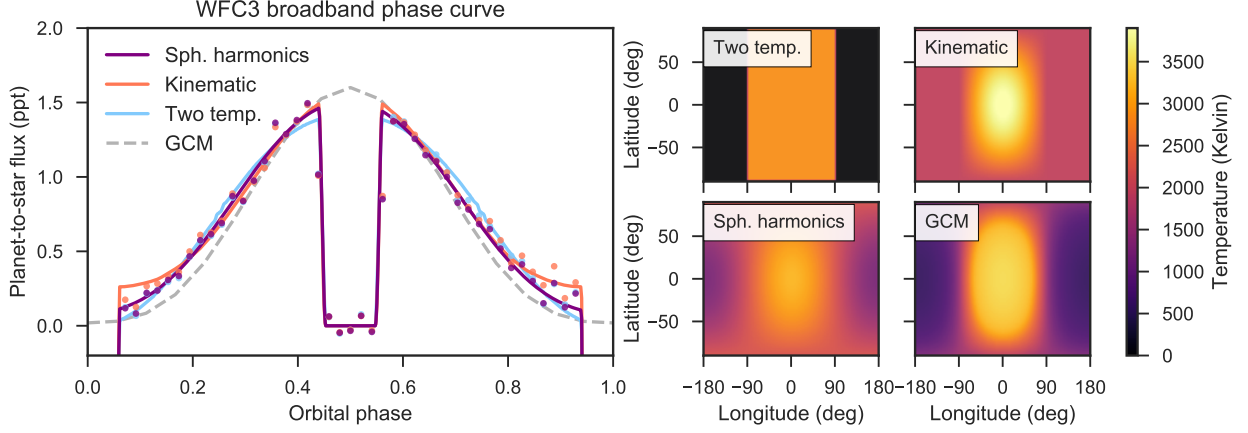


Figure 6. Left: Fits to the broadband WFC3 phase curve compared to a GCM. The colored lines correspond to different temperature maps fit to the data, and the dashed gray line is from the τ_{drag3} GCM. We also show the planet-to-star flux corresponding to each map (points), which is model-dependent due to slight degeneracies with the instrument systematic model. **Right:** Temperature maps from the best fit models and the GCM at a representative photospheric pressure of 0.01 bar.

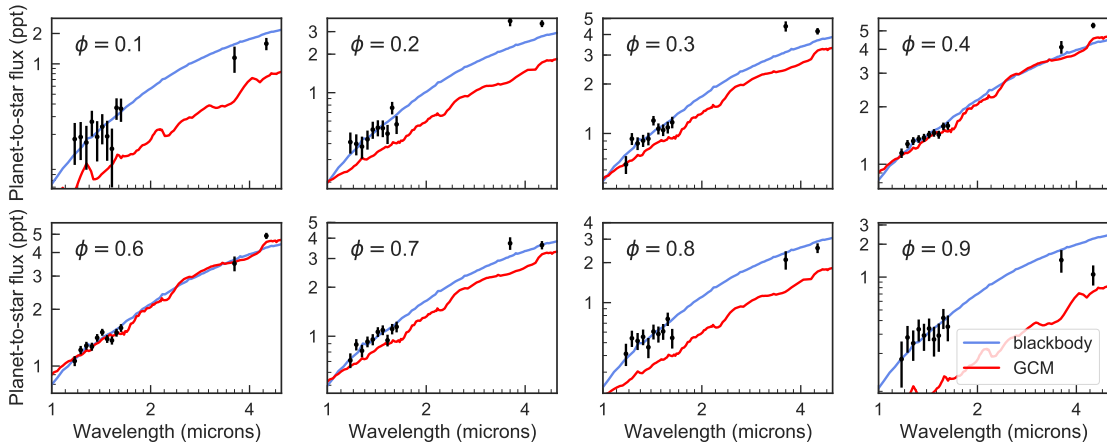


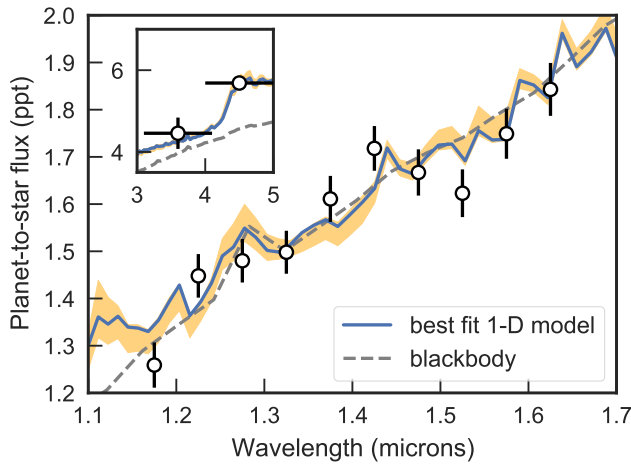
Figure 7. Phase-resolved emission spectra (points) compared to the best fit blackbody (blue line) and the GCM with τ_{drag3} s. Phases $\phi = 0.5$ and 0.0 are centered on the substellar and anti-stellar points, respectively.

We fit three different models to characterize the planet’s climate: a two-temperature map, the physically-motivated kinematic model of (Zhang & Showman 2017), and a spherical harmonic map. We also fit the thermal phase variation with a sinusoid, which can be inverted to map the climate (Cowan & Agol 2008). All of the models provide reasonable fits to the data, with χ^2_ν near unity, but they yield significantly different temperature maps. Table 4 lists the minimum and maximum temperatures for the best fit models to the WFC3 broadband and two Spitzer phase curves. We also list the information criterion (BIC) and Akaike information criterion (AIC) values for the fits (a ΔBIC value greater than 10 constitutes strong evidence against a given model; Kass & Raftery 1995).

The best fit model is either a sinusoid or spherical harmonics, depending on which criterion is used for model selection. The BIC generally favors the simpler spherical harmonics model because it penalizes model complexity relatively more than the AIC (Kass & Raftery 1995). The sinusoid has eight free parameters (amplitude, phase offset, eclipse duration, ingress/egress duration, and midpoint and depth for each of two eclipses), whereas the spherical harmonics model has four (for degree two). The kinematic and two temperature models tend to perform significantly worse (ΔBIC and ΔAIC greater than 10). As illustrated in Figure 6, the kinematic model overpredicts the nightside flux, whereas the two temperature model overpredicts the flux at quadrature and underpredicts the dayside.

Table 2. Phase Curve Properties

Bandpass	Source	Amplitude	Offset (Degrees)
WFC3	data	0.91 ± 0.02	-0.3 ± 0.1
	nominal GCM	0.89	15.32
	[Fe/H] = 0.5 GCM	0.84	19.64
	τ_{drag4} GCM	0.97	2.34
	τ_{drag3} GCM	0.99	0.18
Spitzer 3.6 μm	data	0.86 ± 0.13	2.0 ± 0.7
	nominal GCM	0.78	9.19
	[Fe/H] = 0.5 GCM	0.72	12.79
	τ_{drag4} GCM	0.86	0.90
	τ_{drag3} GCM	0.97	0.18
Spitzer 4.5 μm	data	0.83 ± 0.05	1.0 ± 0.4
	nominal GCM	0.79	8.11
	[Fe/H] = 0.5 GCM	0.73	11.35
	τ_{drag4} GCM	0.85	0.90
	τ_{drag3} GCM	0.93	0.18

**Figure 8.** Dayside emission spectrum (points) compared to the best fit 1-D model (blue line) with 1σ uncertainty shaded in orange. We also show the best fit blackbody (fit to the WFC3 data only).

We compared the planet’s minimum and maximum temperature for the three climate maps by computing the temperatures over a 100×100 grid in latitude and longitude. The kinematic model has the hottest

dayside temperature and the two-temperature model has the smallest. The differences in peak temperature for the models we consider ranges from 630 K for *Spitzer* Channel 1 to 1070 K for the broadband WFC3 light curve. The minimum nightside temperature is also model-dependent: for the WFC3 data, the two-temperature model predicts a nightside temperature of zero Kelvin, whereas the best fit kinematic model has a nightside temperature of 1980 K. These differences arise because the kinematic model allows a steep temperature gradient on the dayside, so the substellar point is much hotter than the terminator, whereas the two temperature map imposes a constant dayside temperature. The spherical harmonics model has an intermediate temperature gradient, and fits the data the best. However, this model may not be physically realistic: on the nightside, it produces higher temperatures at the poles than at the equator, contrary to predictions from GCMs (which we discuss in § 6).

4.4. Comparison with Previous Observations

We compared our results to the dayside emission spectrum reported by [Cartier et al. \(2017\)](#), which is based on a Gaussian process analysis of two secondary eclipses from *HST*/WFC3. The shape of their spectrum is consistent with what we find, but their eclipse depths are 125 ppm smaller on average. In their analysis, [Cartier et al. \(2017\)](#) noted that the Gaussian process fit produces smaller eclipse depths than a parametric fit (also by 125 ppm). One explanation for this difference is that the Gaussian process models some of the astrophysical signal. If the planet’s thermal phase variation is absorbed into the instrument systematic model, the measured eclipse depths would be lower by about 100 ppm. Since our analysis accounts for the thermal phase variation, it is more likely to provide a robust estimate of the secondary eclipse depths. Our estimated uncertainties are a factor of four smaller than those reported in [Cartier et al. \(2017\)](#), which is consistent with photon-limited expectations (our data set includes two additional eclipses, a factor of five longer out-of-eclipse baseline, and has 60% larger wavelength bins).

We also compared our dayside spectrum to the z' and K_S -band secondary eclipse depths reported in [Delrez et al. \(2018\)](#). The z' eclipse is 1.0σ lower than our best fit blackbody spectrum (described in § 5), and the K_S measurement is higher than the model by 2.5σ . Since these results are consistent with (but less precise than) the WFC3 data, we do not include them in our analysis of the atmospheric composition, but we encourage additional measurements in the K_S band to confidently de-

Table 3. Phase-Resolved Emission Spectra

λ	Dilution	$\phi = 0.1$	$\phi = 0.2$	$\phi = 0.3$	$\phi = 0.4$	$\phi = 0.5$	$\phi = 0.6$	$\phi = 0.7$	$\phi = 0.8$	$\phi = 0.9$
1.175	0.10	179 ± 79	411 ± 77	647 ± 80	1143 ± 65	1259 ± 47	1063 ± 64	710 ± 73	412 ± 78	177 ± 79
1.225	0.11	188 ± 76	398 ± 74	928 ± 77	1276 ± 62	1448 ± 46	1216 ± 62	888 ± 71	539 ± 75	280 ± 76
1.275	0.11	166 ± 76	379 ± 74	869 ± 77	1323 ± 62	1480 ± 46	1282 ± 62	814 ± 71	515 ± 75	247 ± 76
1.325	0.11	266 ± 75	432 ± 73	904 ± 76	1357 ± 62	1498 ± 45	1267 ± 61	925 ± 70	552 ± 74	333 ± 75
1.375	0.12	189 ± 81	514 ± 78	928 ± 82	1376 ± 66	1611 ± 48	1411 ± 65	954 ± 75	461 ± 79	292 ± 81
1.425	0.13	238 ± 79	532 ± 76	1198 ± 79	1431 ± 64	1718 ± 47	1511 ± 64	1063 ± 73	605 ± 77	338 ± 79
1.475	0.14	191 ± 81	527 ± 79	1068 ± 82	1460 ± 66	1667 ± 48	1392 ± 66	1090 ± 75	580 ± 80	268 ± 81
1.525	0.14	143 ± 84	478 ± 81	1048 ± 85	1429 ± 69	1623 ± 50	1367 ± 68	943 ± 77	607 ± 82	291 ± 84
1.575	0.15	367 ± 88	761 ± 85	1088 ± 89	1581 ± 72	1749 ± 52	1503 ± 71	1107 ± 81	754 ± 86	422 ± 88
1.625	0.16	359 ± 93	565 ± 90	1169 ± 94	1590 ± 76	1843 ± 56	1593 ± 75	1142 ± 86	542 ± 91	351 ± 93
3.6	0.17	1148 ± 333	3633 ± 330	4487 ± 320	4107 ± 314	4458 ± 383	3495 ± 315	3720 ± 330	2102 ± 331	1431 ± 334
4.5	0.16	1586 ± 220	3468 ± 214	4188 ± 190	5334 ± 179	5686 ± 138	4904 ± 183	3626 ± 214	2575 ± 217	1057 ± 221

Table 4. Model Comparison

Data	Model	T_{\min}	T_{\max}	Δ_{AIC}	Δ_{BIC}
WFC3	Sph. Harmonics	1214	3251	0.0	0.0
	Kinematic	1980	3958	11.8	11.8
	Two Temp.	0	2887	47.7	43.2
	Sinusoid	–	–	17.7	13.2
Ch 1	Sph. Harmonics	1280	3444	48.0	0.0
	Kinematic	1955	3675	82.3	34.3
	Two Temp.	1429	3041	58.7	17.6
	Sinusoid	–	–	0.0	98.4
Ch 2	Sph. Harmonics	902	3786	2.2	3.1
	Kinematic	1703	4276	16.55	17.41
	Two Temp.	1361	3311	26.1	0.0
	Sinusoid	–	–	0.0	49.6

termine whether an emission feature is present at those wavelengths.

5. ATMOSPHERIC COMPOSITION AND THERMAL STRUCTURE

We characterized the planet’s atmospheric composition by fitting 1D models to the phase-resolved emission spectra. First, we modeled the planet flux as a simple blackbody to estimate the dayside brightness tem-

perature and test for significant absorption or emission features. We then performed a more sophisticated grid-based retrieval to estimate the atmospheric metallicity, carbon-to-oxygen ratio, and thermal structure.

5.1. Blackbody Fits

A blackbody is the simplest model for the planet’s thermal emission and provide a useful first evaluation of the atmospheric properties. The best fit blackbodies are shown in Figures 7 and 8. This model performs well for some orbital phases, with χ^2_{ν} ranging from 0.9 to 1.1 for phases $\phi = 0.1, 0.7$ and 0.8. At other phases the blackbody model is a poorer fit, particularly to the *Spitzer* data. For phases 0.2 – 0.6, the *Spitzer* eclipse depths are significantly larger than predicted for the best fit blackbody, suggesting the presence of an emission feature. On the nightside (phase 0.9), the *Spitzer* 4.5 μm eclipse depth is *smaller* than predicted, suggesting an absorption feature. These differences indicate changes in thermal structure with longitude in the atmosphere.

We also fit blackbody models to the WFC3 data only, and found that they provide a good fit at all orbital phases. The χ^2_{ν} values range from 0.5 to 1.6, with a median of 0.9. The best fit effective temperatures range from 1920 Kelvin on the nightside to 2980 Kelvin on the dayside. We report the best fit temperatures with uncertainties in Table 5. The dayside spectrum is the poorest fit by the blackbody model. This finding is not a surprise because the dayside has higher signal-to-noise than the other orbital phases, thanks to the two secondary eclipse observations from [Cartier et al. \(2017\)](#).

Table 5. Phase-resolved Effective Temperature

Orbital Phase	T_{eff}	χ^2_ν
0.06 – 0.15	1919 ± 40	0.6
0.15 – 0.25	2256 ± 24	0.8
0.25 – 0.35	2651 ± 17	1.2
0.35 – 0.44	2906 ± 11	0.8
0.44 – 0.56	3013 ± 8	1.6
0.56 – 0.65	2885 ± 12	1.3
0.65 – 0.75	2636 ± 16	0.9
0.75 – 0.85	2313 ± 23	1.1
0.85 – 0.94	2027 ± 36	0.5

The more sophisticated grid-based retrieval (described in the next section) provides a better fit to the dayside.

5.2. Grid-Based Retrieval

Since the phase-resolved spectra do not show spectrally resolved molecular features, we opted for a simple grid-based fit to the planet’s atmospheric properties, similar to the grid search used in [Arcangeli et al. \(submitted\)](#); [Mansfield et al. \(submitted\)](#). We generated a grid from one-dimensional forward models of the atmosphere over a broad range of metallicities, carbon-to-oxygen ratios (C/O), and stellar irradiation. The stellar spectrum is scaled in intensity over the grid to model the unknown heat redistribution for the planet; i.e., a lower dayside irradiation is equivalent to more efficient heat transport to the nightside.

At each point in the grid, we compute forward models to determine self-consistent, radiative-convective temperature-pressure (T-P) profiles. We determine the molecular abundances in each atmospheric layer assuming thermochemical equilibrium (calculated with the NASA CEA routine; [Gordon & McBride 1994](#)). We include opacity from the major absorbers expected for a hot Jupiter atmosphere, including H_2O , CO , CO_2 , TiO , VO , FeH , and $\text{H}_2\text{-H}_2$ CIA. Notably, in contrast to many previous studies of the hottest planets, we also included opacity from H- , which is an important absorber at temperatures above 2500 K ([Arcangeli et al. submitted](#)). Using these opacities and T-P profiles, we calculated thermal emission spectra over the full grid using the CHIMERA retrieval suite (described in [Line et al. 2013, 2014](#)). We then explored the grid with an MCMC chain using the `emcee` package ([Foreman-Mackey et al. 2013](#))

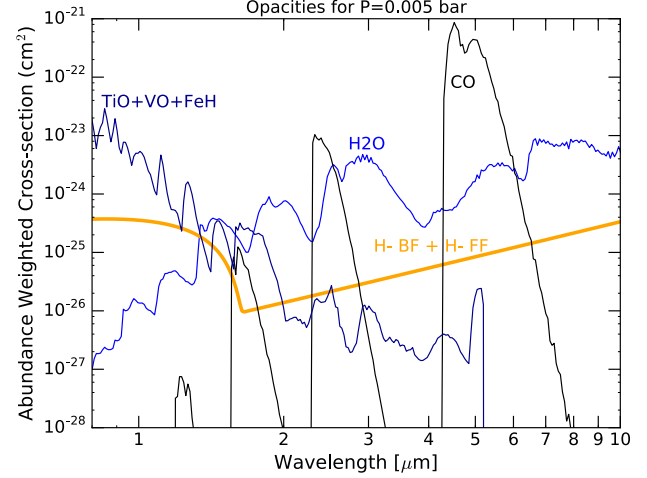


Figure 9. Abundance weighted absorption cross-sections illustrating the important opacity sources at the photospheric pressure level (5 mbar). The strong CO feature at $4.5\,\mu\text{m}$ contributes to the high planet-to-star flux at that wavelength. Water, hydrides/oxides, and the H- bound-free opacities all play a role in shaping the *HST*/WFC3 spectrum.

and interpolated in the grid to calculate the likelihood at each model step. We fit this model to the dayside and nightside emission spectra (phases $\phi = 0.5$ and 0.1).

5.2.1. Dayside Spectrum

The main characteristics of the dayside emission spectrum are: (1) it is blackbody-like at WFC3 wavelengths, and (2) in the *Spitzer* bands, the planet-to-star flux is significantly higher than predicted for the best fit blackbody, indicating an emission feature. The best fit spectrum reproduces these data fairly well, with $\chi^2_\nu = 1.77$. The largest contribution to the χ^2 value is the $4.5\,\mu\text{m}$ eclipse depth, which is larger than the best fit model prediction by 2.9σ . When the $4.5\,\mu\text{m}$ point is removed, the fit has $\chi^2_\nu = 1.17$. The best fit model has a moderately enhanced metallicity ($23\times$ solar), carbon-to-oxygen equal to 0.76, poor heat redistribution, and a thermal inversion (temperature increasing with altitude).

Figure 9 shows the opacity contributions of key absorbers for the best fit model. In the optical (which we do not observe directly), there is strong absorption by TiO , VO , and FeH . In the near-infrared, H_2O , H- , and hydrides/oxides all contribute to the opacity, leading to nearly constant opacity over the WFC3 wavelength range. In cooler atmospheres, water is the dominant absorber over this bandpass (e.g. [Kreidberg et al. 2014b; Line et al. 2016](#)), but in WASP-103b, H_2O is partially dissociated in the photosphere, leading to a drop in abundance by a factor of ~ 10 (see Figure 10). Wa-

ter also has intrinsically weaker features at high temperature (Tinetti et al. 2012). Water is also an efficient coolant, so lower water abundance leads to a more isothermal photosphere, which further weakens the contrast in and out of the water band. On top of this, there is significant H- opacity from single H atoms bound with free electrons, which fills in the opacity at wavelengths shorter than $1.5 \mu\text{m}$. Taken together, all these factors conspire to produce a nearly featureless spectrum from $1.1 - 1.7 \mu\text{m}$. Finally, in the infrared the dominant absorber is CO, which produces the emission feature at *Spitzer* wavelengths.

Figure 10 shows a summary of the temperature-pressure profile and abundances for the best fit model. The T-P profile is inverted, with temperature increasing from 2800 to 3500 K over the pressure range $10^{-2} - 10^{-3}$ bar. The thermal inversion is driven by absorption of optical light by oxides and hydrides in the upper atmosphere. The observations are sensitive to pressures of $\sim 0.01 - 0.001$ bar, which spans the tropopause, where temperature begins to increase and the water abundance drops by more than an order of magnitude.

In Figure 11, we show the posterior distributions from the grid retrieval. We infer a range in metallicity of $23_{-13}^{+29} \times$ solar, somewhat higher than expected based on Jupiter’s metal enrichment ($3 - 5 \times$ solar; Wong et al. 2004) and the trend toward decreasing metallicity with increasing planet mass observed for the Solar System and exoplanets (e.g. Kreidberg et al. 2014b). However, planet population synthesis models predict some scatter in atmospheric metallicity. Planets near WASP-103b’s mass ($1.5 M_{\text{Jup}}$) are expected to have metallicities ranging from roughly $1 - 10 \times$ solar (Mordasini et al. 2016). Our result for WASP-103b lies on the upper end of this range, and may be indicative of intrinsic scatter in the mass-atmospheric metallicity relation.

The retrieved C/O is consistent with solar, with a 1σ confidence interval of $0.54 - 0.85$. We infer an upper limit on C/O of 0.9 at 3σ confidence, driven by the fact that the atmospheric chemistry is expected to change dramatically when C/O exceeds unity. For a carbon-rich composition, the equilibrium abundance of methane relative to CO increases by orders of magnitude compared to an oxygen-rich composition (e.g. Madhusudhan et al. 2011). Our *Spitzer* eclipse depths are sensitive to the relative abundance of these species, so we can confidently rule out a carbon-rich composition despite the lack of spectrally resolved features.

We infer a heat redistribution $f = 0.4_{-0.02}^{+0.03}$. The f parameter is allowed to range from 0 (isotropic heat distribution) to 0.5 (dayside emission only). Our estimate of f is close to the maximum, indicating inefficient trans-

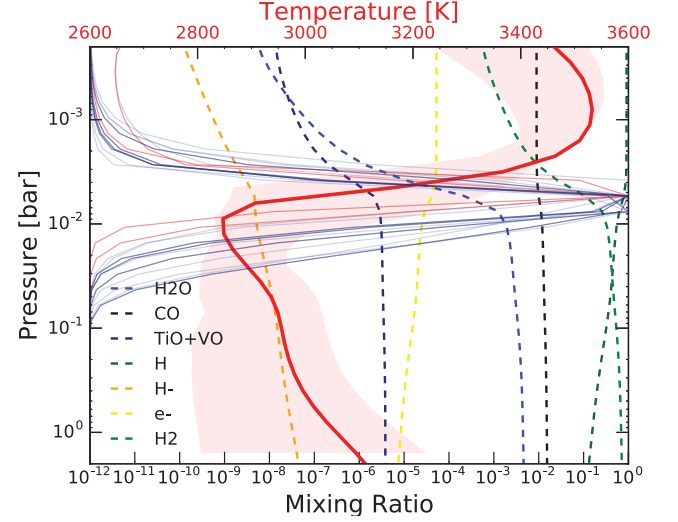


Figure 10. Summary of the 1D self-consistent model atmosphere fits. The temperature-pressure profile (top axis) is indicated by the 1-sigma spread of 500 randomly drawn T-P profiles from the posterior (light red) and a representative fit, with $f=0.4$, $[M/H]=1.5$, and $C/O=0.7$ (dark red). The normalized thermal emission contribution functions for the *Spitzer* points are shown in solid red, the WFC3 in-water band ($1.33 - 1.48 \mu\text{m}$) in dark blue, and WFC3 out-of-water-band in light blue. The observations probe between ~ 0.01 and 0.001 bar, just above the tropopause region of the atmosphere where the temperature is increasing. The dashed curves are thermochemical equilibrium mixing ratios for important absorbers computed along the representative fit’s self-consistent T-P profile. Note the rapid dissociation of water above the ~ 10 mbar level where the inversion begins.

port of heat to the nightside. Poor heat transport is observed in other very hot planets as well, due to damping of heat-propagating waves by fast radiative cooling or frictional drag in a partially ionized atmosphere (Komacek et al. 2017). The heat redistribution is correlated with atmospheric metallicity because increasing metallicity pushes the photosphere to higher pressure levels.

We note that an important caveat for our results is that the best fit model is not a perfect fit to the data (with $\chi_\nu = 1.77$), so the uncertainties produced by the MCMC may be underestimated. Furthermore, the inferred C/O and metallicity are highly sensitive to the planet-to-star flux at *Spitzer* $4.5 \mu\text{m}$, which is the worst fit data point. To fit this data point, the model favors super-solar metallicities and C/O, which drive up the CO abundance (the dominant absorber at $4.5 \mu\text{m}$). Given that the result hinges on a single photometric band and there are no spectrally resolved molecular features to constrain the temperature-pressure profile or which absorbers are present, we caution against over-

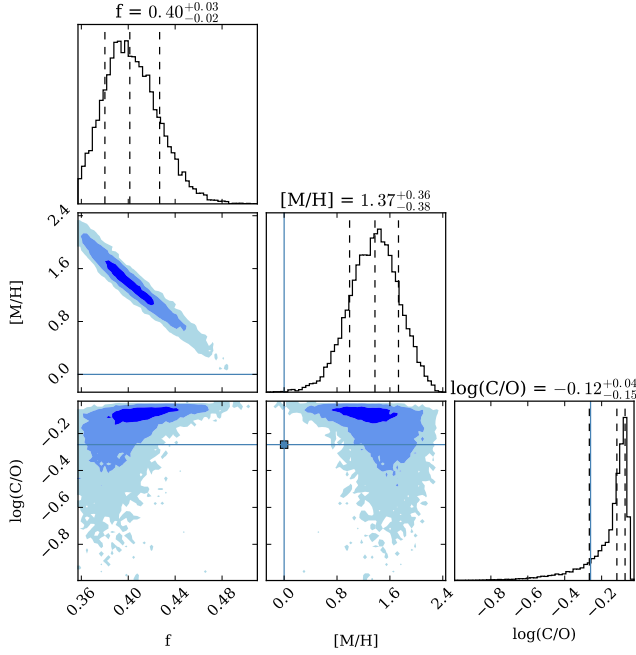


Figure 11. Posterior distributions for WASP-103b’s atmospheric heat redistribution, metallicity, and C/O, from a grid-based fit to the dayside emission spectrum. The histograms on the diagonal show the marginalized distribution of each parameter, with dashed lines indicating the median and surrounding 68% credible interval. The blue lines correspond to solar metallicity (1) and C/O (0.54). The 2D histograms mark the 1, 2, and 3 σ credible regions in dark, medium, and light blue, respectively.

interpreting these results until wider spectral coverage is available.

5.2.2. Nightside Spectrum

We also fit the nightside spectrum (phase 0.1) with the grid-based retrieval. The best fit spectrum has a non-inverted temperature pressure profile. At 1 σ confidence, the metallicity is 15 – 240 \times solar and the C/O is unbounded over the full prior range (**Mike: what priors did you use?**). The atmospheric composition is consistent with results from the dayside spectrum.

This agreement is an encouraging sanity check; however, there are several model assumptions that may result in artificially tight constraints on the atmospheric properties. One challenge in modeling the nightside spectrum is that the shape of the T-P profile is unknown. Our model assumes a scaled stellar irradiation at the top of the atmosphere, but in reality, the heat source is advection from the dayside. Another caveat is that the model is not self-consistent: the energy leaving the dayside is not constrained to equal the energy en-

tering the nightside. Further work is needed to develop a fully self-consistent 2-D retrieval method.

6. COMPARISON WITH GCMs

To explore the three-dimensional effects of atmospheric dynamics, we ran several GCM models to compare with the measured phase-resolved spectra. (**Vivien: add text describing GCM**). Our nominal GCM was a cloud-free, solar composition atmosphere with TiO/VO opacity and no added drag. We also ran models with enhanced metallicity ([Fe/H] = 0.5), no TiO/VO, and added atmospheric drag. Lorentz drag can occur in the hottest exoplanet atmospheres, which may be partially ionized and coupled to the background magnetic field. We parameterized the drag (**Vivien: how did you model drag?**), with timescales of $\tau_{\text{drag}} = 10^3$ and 10^4 s. We label the drag models $\tau_{\text{drag}3}$ and $\tau_{\text{drag}4}$, respectively.

To assess how well the GCM predictions reproduce the data, we calculated the amplitude and hot spot offset for all the models (listed in Table 2). The observed hotspot offsets (0.3 – 2.0 degrees) are best reproduced by the $\tau_{\text{drag}3}$ and $\tau_{\text{drag}4}$ models, which have small offsets due to slower wind speeds. The nominal and metal-enhanced GCMs both have offsets that are too large (10-20 degrees). On the other hand, the drag models do not match the observed phase curve amplitudes (with values near unity, in contrast to the 0.8 - 0.9 that is observed). As shown in Figure 12, the drag models predict the dayside planet-to-star flux fairly accurately, but underestimate the planet-to-star flux away from the sub-stellar point. (**Vivien and others: how do we heat up the nightside to match the data better?**)

We also compared the GCM output to temperature maps retrieved with **spiderman**. Figure 6 shows the 0.01 bar temperature map for the $\tau_{\text{drag}3}$ GCM compared to the best fit models. At this pressure, the GCM has minimum and maximum temperatures of 580 and 3520 K. The temperature gradient from the dayside to the terminator is intermediate between the kinematic and spherical harmonics models. The GCM predicts a cooler nightside than all models except the two-temperature model. We note that the GCM does not provide a perfect fit to the data, whereas multiple **spiderman** maps fit quite well, with large differences in temperature between them (see Table 4). Determining which models (if any) accurately describe the climate will require higher precision phase curves and/or eclipse mapping (e.g. de Wit et al. 2012).

The GCMs also provide insight into what molecules are present in which parts of the atmosphere. As discussed in § 5, water dissociation and H- opacity are

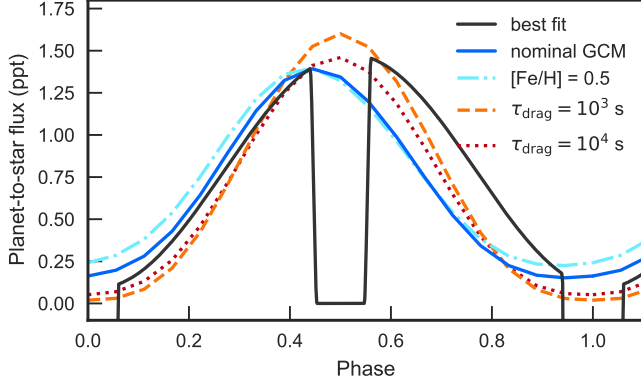


Figure 12. GCM predictions (colored lines) compared to the best fit model for the WFC3 white light phase curve (black line). The nominal model is solar composition, cloud-free, with TiO/VO opacity and no drag. The models are corrected for the predicted ellipsoidal variability of the planet.

needed to explain the dayside emission spectrum. Figure 12 shows the photospheric abundances of H_2O and H - compared to the predicted temperature for the $\tau_{\text{drag}3}$ GCM. The water abundance drops by ~ 10 at the sub-stellar point, and the H - opacity increases by ~ 100 . By contrast, CO remains intact throughout the atmosphere. Our observations are not precise enough to detect water features on the nightside of the planet (see §7, but future high precision data may be sensitive to these features, and will help constrain the strength of horizontal transport in the atmosphere (Agúndez et al. 2014).

7. COMPARISON WITH BROWN DWARFS AND DIRECTLY IMAGED COMPANIONS

WASP-103b is so highly irradiated that its photospheric temperature (2000 – 3000 K) is comparable to that of low mass stars. However, the planet’s other properties (surface gravity, rotation rate, irradiation) are different. To explore the effects of varying these parameters, we compared the spectra of WASP-103b to brown dwarfs and young directly imaged companions. The object properties are summarized in Table 6.

We selected spectra from WASP-103b at three orbital phases: dayside ($\phi = 0.5$), quadrature ($\phi = 0.25$), and nightside ($\phi = 0.1$), and compared them to sources with comparable effective temperature. Figure 14 shows the flux-calibrated spectra (assuming a distance of 10 pc). The directly imaged spectra are taken from Wahhaj et al. (2011); Aller et al. (2013); Bonnefoy et al. (2014). They are calibrated in absolute flux using published H-band photometry (Wahhaj et al. 2011; Bonnefoy et al. 2009; Aller et al. 2013) and distances (Gaia Collaboration et al. 2016), a flux-calibrated spectrum of Vega (Mountain et al. 1985; Hayes 1985), and the correspond-

ing filter passbands. The brown dwarf spectra **Jackie: describe catalog of brown dwarf spectra and flux calibration.**

The main spectral feature over the wavelength range we consider is water. To quantitatively compare the water feature amplitude for different objects, we define an amplitude $A = (F_{\lambda_1, \lambda_2} - F_{\lambda_3, \lambda_4}) / F_{\lambda_1, \lambda_2}$, where F_{λ_x, λ_y} is the weighted mean flux in a wavelength bin $x - y$. We calculated the water feature amplitude for two choices of wavelength bins. For the first, A_1 , we considered data in and out of the water band, with $\lambda_{1,2,3,4} = 1.15, 1.3, 1.35, 1.5 \mu\text{m}$. The ground-based direct imaging data doesn’t span this entire wavelength, so we also define an amplitude A_2 with $\lambda_{1,2,3,4} = 1.2, 1.35, 1.5, 1.65 \mu\text{m}$. The estimated amplitudes and uncertainties are listed in Table 6.

For WASP-103b, A_1 is consistent with zero at all three orbital phases. The brown dwarfs have similar

8. SUMMARY

We observed thermal phase curves of the hot Jupiter WASP-103b measured with *HST*/WFC3 time series spectroscopy (1.15 – 1.65 μm) and *Spitzer*/IRAC broadband photometry (3.6 and 4.6 μm bands).

- The phase curves have large amplitudes ($0.8 - 0.9 \times$ the secondary eclipse depth), and small offsets in peak brightness from the substellar point (consistent with zero degrees at all wavelengths). These characteristics indicate inefficient redistribution of heat to the nightside, as seen in other very hot Jupiters (Komacek et al. 2017).
- We fit the phase variation with the **spiderman** package (Louden & Kreidberg 2017) to evaluate different models of the planets climate. A spherical harmonic temperature map generally provides the best fit to the data; however, all the maps produce reasonable fits (χ^2_ν near unity), and there are large differences in temperature between them (> 1000 K). Breaking the degeneracy between different climate maps will require higher precision phase curves and/or secondary eclipse mapping (e.g. de Wit et al. 2012).
- We calculated phase-resolved spectra in ten orbital phase bins. The *HST*/WFC3 spectra are consistent with blackbody emission from the planet at all orbital phases. The best fit effective temperatures ranges from 1920 K (phase $\phi = 0.1$) to 3010 K on the dayside. We attribute the absence of water features at WFC3 wavelengths to (1) H_2O dissociation on the dayside, (2) additional near-IR opacity from H -, TiO/VO and FeH, (3) a small

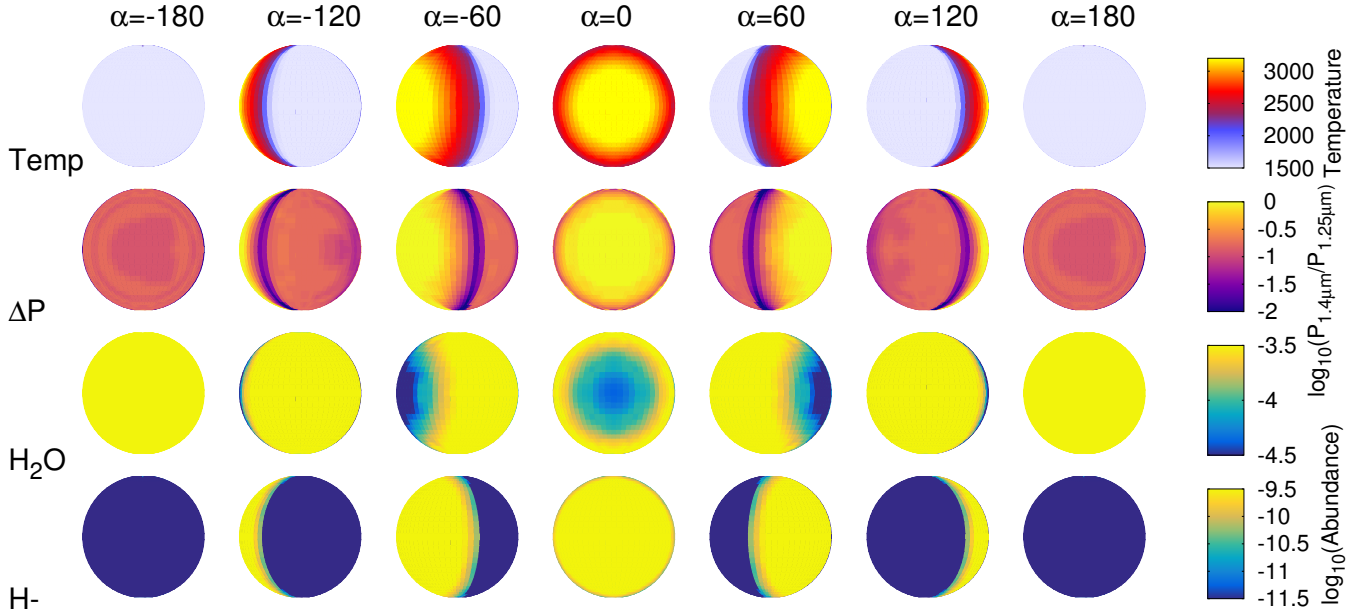


Figure 13. Row (1): photospheric temperatures for the τ_{drag3} GCM for different viewing geometries. The substellar point corresponds to $\alpha = 0$ and the antistellar point is $\alpha = \pm 180$. Row (2) indicates the ratio of pressures probed in and out of the water band. On the dayside, the opacity out of the water band is filled in by absorption from H- and TiO/VO. Rows (3-4) show the abundances of H₂O and H-. The dayside temperatures, water dissociates and the photospheric abundance drops by ~ 10 .

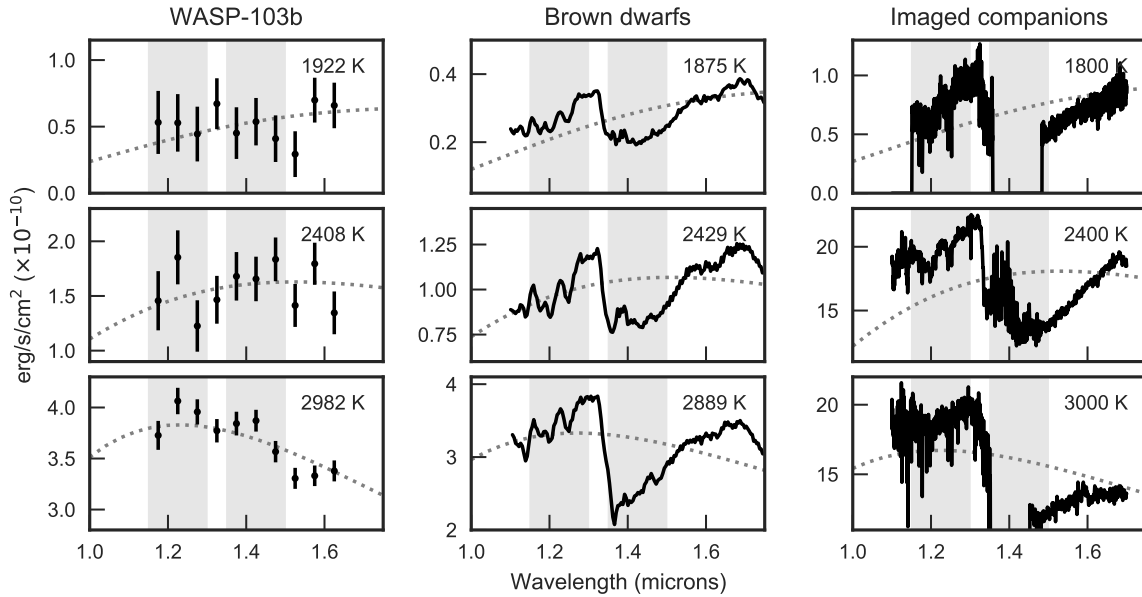


Figure 14. Flux-calibrated spectra for WASP-103b (left column) compared to brown dwarfs (middle) and directly imaged companions (right), assuming a distance of 10 pc. The WASP-103b spectra are from the nightside (phase 0.1, top row), quadrature (phase 0.25, middle) and the dayside (phase 0.5, bottom). Each row shows spectra from objects of comparable temperature. The dotted gray line corresponds to the best fit blackbody. Effective temperatures are listed in the upper right corners. The wavelength bins used to calculate the water feature amplitude A_1 are shaded in gray.

Table 6. Source Properties

	Object	T_{eff}	$\log g$	H ₂ O A ₁	H ₂ O A ₂
Hot Jupiter	W103b night	1922 ± 40	3.2 ± 0.04	$0.07 \pm 1.8\text{e} - 01$	$-0.00 \pm 1.6\text{e} - 01$
	W103b quadrature	2408 ± 20	3.2 ± 0.04	$-0.14 \pm 7.8\text{e} - 02$	$-0.01 \pm 6.7\text{e} - 02$
	W103b dayside	2982 ± 10	3.2 ± 0.04	$0.04 \pm 1.4\text{e} - 02$	$0.15 \pm 1.2\text{e} - 02$
Brown Dwarf	2MASS J1320+0409	1875 ± 70	5.19 ± 0.16	$0.21 \pm 6.3\text{e} - 04$	$-0.06 \pm 5.0\text{e} - 04$
	2MASS J0428-2253	2429 ± 80	5.22 ± 0.09	$0.16 \pm 1.2\text{e} - 04$	$-0.03 \pm 1.0\text{e} - 04$
	2MASS J0003-2822	2889 ± 80	5.18 ± 0.04	$0.26 \pm 1.3\text{e} - 04$	$0.10 \pm 1.1\text{e} - 04$
Imaged Companion	CD-35 2722 ¹	1800 ± 100	4.5 ± 0.5	—	$0.15 \pm 1.0\text{e} - 05$
	USco 1610-1913B ²	2400 ± 150	—	$0.27 \pm 2.0\text{e} - 04$	$0.19 \pm 2.2\text{e} - 04$
	TWA 22A ³	3000 ± 100	4.5 ± 0.5	—	$0.29 \pm 2.0\text{e} - 05$

¹Wahhaj et al. (2011)²Aller et al. (2013)³Bonnefoy et al. (2014)

temperature gradient at the pressure levels probed by the data. The *Spitzer* data are *not* consistent with a blackbody: there is an infrared emission feature at phases where the substellar point is visible ($\phi = 0.2 - 0.7$), which transitions to an absorption feature on the nightside ($\phi = -0.1 - 0.1$). We attribute these features to CO and changing thermal structure from the dayside to the nightside.

- We characterized the composition with a 1D grid-based retrieval that assumes thermochemical and radiative-convective equilibrium. The atmosphere is moderately metal-enriched ($23_{-13}^{+29} \times$ solar; and $> 1 \times$ solar at 3σ confidence). This value is somewhat higher than what is observed for other gas giants and predicted by models (e.g. Wong et al. 2004; Kreidberg et al. 2014b; Mordasini et al. 2016), and may be indicative of intrinsic scatter in the relationship between atmospheric metallicity and planet mass. However, the metallicity is strongly sensitive to the $4.5 \mu\text{m}$ *Spitzer* eclipse depth, and additional observations would be useful in confirming the metal enhancement. In addition to metallicity, we also infer an upper limit on the carbon-to-oxygen ratio of 0.9 (3σ confidence). This estimate agrees with expectations from planet formation models that pollution from water ice in planetesimals leads to $\text{C/O} < 1$ in gas giant atmospheres (Mordasini et al. 2016; Espinoza et al. 2017). The best fit temperature pressure profile has a thermal inversion from $\sim 10^{-2} - 10^{-3}$ bars due to TiO/VO absorption at high altitudes.
- We ran several 3D GCMs to compare to the data, including a nominal model with a cloud-free, so-

lar composition, a metal-enriched model ($[\text{Fe}/\text{H}] = 0.5$), and two models with Lorentz drag. The GCMs with Lorentz drag have slower wind speeds and provide the best match to the data small hotspot offsets that are observed, but they underpredict the planet's nightside flux.

- We compared the spectra of WASP-103b at phases 0.5 (dayside), 0.25 (quadrature), and 0.1 (nightside) to brown dwarfs and directly imaged companions of similar temperature. Both the brown dwarfs and imaged companions show evidence for water features, as defined by FIXME spectral index. Cite Beatty

Future observations with JWST planets are round and complicated

The data presented in this paper were obtained from the Mikulski Archive for Space Telescopes (MAST) and the NASA/IPAC Infrared Science Archive. STScI is operated by the Association of Universities for Research in Astronomy, Inc., under NASA contract NAS5-26555. The Infrared Science Archive is operated by the Jet Propulsion Laboratory, California Institute of Technology, under contract with the National Aeronautics and Space Administration. This work also made use of the Python packages SciPy and NumPy (Jones et al. 2001; Van Der Walt et al. 2011). The authors are grateful for helpful conversations with Caroline Morley, Thomas Beatty, Ming Zhao, Kim Star Cartier, Hannah Diamond-Lowe, and Nick Cowan. We also thank the organizers of the 2016 Santa Cruz Kavli Summer Program and the 2017 Ringberg Atmospheres of Disks and Planets meeting for facilitating many discussions and collaborations.

REFERENCES

- Agúndez, M., Parmentier, V., Venot, O., Hersant, F., & Selsis, F. 2014, *A&A*, 564, A73
- Aller, K. M., Kraus, A. L., Liu, M. C., et al. 2013, *ApJ*, 773, 63
- Arcangeli, J., Désert, J. M., Line, M., et al. submitted, Submitted to *ApJL*
- Armstrong, D. J., de Mooij, E., Barstow, J., et al. 2016, *Nature Astronomy*, 1, 0004
- Beatty, T. G., Madhusudhan, N., Pogge, R., et al. 2017a, *AJ*, 154, 242
- Beatty, T. G., Madhusudhan, N., Tsiraras, A., et al. 2017b, *AJ*, 154, 158
- Bonnefoy, M., Chauvin, G., Lagrange, A.-M., et al. 2014, *A&A*, 562, A127
- Bonnefoy, M., Chauvin, G., Dumas, C., et al. 2009, *A&A*, 506, 799
- Braak, C. J. F. T. 2006, *Statistics and Computing*, 16, 239. <http://dx.doi.org/10.1007/s11222-006-8769-1>
- Carter, J. A., & Winn, J. N. 2009, *ApJ*, 704, 51
- Cartier, K. M. S., Beatty, T. G., Zhao, M., et al. 2017, *AJ*, 153, 34
- Cowan, N. B., & Agol, E. 2008, *ApJL*, 678, L129
- Crossfield, I. J. M., Barman, T., Hansen, B. M. S., Tanaka, I., & Kodama, T. 2012, *ApJ*, 760, 140

- de Wit, J., Gillon, M., Demory, B.-O., & Seager, S. 2012, *A&A*, 548, A128
- Delrez, L., Madhusudhan, N., Lendl, M., et al. 2018, *MNRAS*, 474, 2334
- Demory, B.-O., de Wit, J., Lewis, N., et al. 2013, *ApJL*, 776, L25
- Diamond-Lowe, H., Stevenson, K. B., Bean, J. L., Line, M. R., & Fortney, J. J. 2014, *ApJ*, 796, 66
- Espinoza, N., Fortney, J. J., Miguel, Y., Thorngren, D., & Murray-Clay, R. 2017, *ApJL*, 838, L9
- Evans, T. M., Sing, D. K., Wakeford, H. R., et al. 2016, *ApJL*, 822, L4
- Foreman-Mackey, D., Hogg, D. W., Lang, D., & Goodman, J. 2013, *PASP*, 125, 306
- Gaia Collaboration, Prusti, T., de Bruijne, J. H. J., et al. 2016, *A&A*, 595, A1
- Gillon, M., Anderson, D. R., Collier-Cameron, A., et al. 2014, *A&A*, 562, L3
- Gordon, S., & McBride, B. J. 1994, Computer program for calculation of complex chemical equilibrium compositions and applications, Vol. 1 (National Aeronautics and Space Administration, Office of Management, Scientific and Technical Information Program)
- Hayes, D. S. 1985, in *IAU Symposium*, Vol. 111, Calibration of Fundamental Stellar Quantities, ed. D. S. Hayes, L. E. Pasinetti, & A. G. D. Philip, 225–249
- Haynes, K., Mandell, A. M., Madhusudhan, N., Deming, D., & Knutson, H. 2015, *ApJ*, 806, 146
- Henry, G. W. 1999, *PASP*, 111, 845
- Horne, K. 1986, *PASP*, 98, 609
- Hu, R., Demory, B.-O., Seager, S., Lewis, N., & Showman, A. P. 2015, *ApJ*, 802, 51
- Husser, T.-O., Wende-von Berg, S., Dreizler, S., et al. 2013, *A&A*, 553, A6
- Jones, E., Oliphant, T., Peterson, P., & Others. 2001, *SciPy: Open source scientific tools for Python*, .
<http://www.scipy.org/>
- Kass, R. E., & Raftery, A. E. 1995, *Journal of the American Statistical Association*, 90, 773.
<http://amstat.tandfonline.com/doi/abs/10.1080/01621459.1995.10476572>
- Kataria, T., Sing, D. K., Lewis, N. K., et al. 2016, *ApJ*, 821, 9
- Knutson, H. A., Charbonneau, D., Allen, L. E., et al. 2007, *Nature*, 447, 183
- Komacek, T. D., Showman, A. P., & Tan, X. 2017, *ApJ*, 835, 198
- Kreidberg, L. 2015, *PASP*, 127, 1161
- Kreidberg, L., Bean, J. L., Désert, J.-M., et al. 2014a, *Nature*, 505, 69
- . 2014b, *ApJL*, 793, L27
- Kreidberg, L., Line, M. R., Bean, J. L., et al. 2015, *ApJ*, 814, 66
- Leconte, J., Lai, D., & Chabrier, G. 2011a, *A&A*, 536, C1
- . 2011b, *A&A*, 528, A41
- Lendl, M., Cubillos, P. E., Hagelberg, J., et al. 2017, *A&A*, 606, A18
- Line, M. R., Knutson, H., Wolf, A. S., & Yung, Y. L. 2014, *ApJ*, 783, 70
- Line, M. R., Wolf, A. S., Zhang, X., et al. 2013, *ApJ*, 775, 137
- Line, M. R., Stevenson, K. B., Bean, J., et al. 2016, *AJ*, 152, 203
- Loeb, A., & Gaudi, B. S. 2003, *ApJL*, 588, L117
- Long, K. S., Baggett, S. M., & MacKenty, J. W. 2015, Persistence in the WFC3 IR Detector: an Improved Model Incorporating the Effects of Exposure Time, Tech. rep.
- Louden, T., & Kreidberg, L. 2017, *ArXiv e-prints*, arXiv:1711.00494
- Madhusudhan, N., Harrington, J., Stevenson, K. B., et al. 2011, *Nature*, 469, 64
- Mansfield, M., Bean, J. B., Line, M., Parmentier, V., & Kreidberg, L. submitted, Submitted to *ApJ*
- McCullough, P., & MacKenty, J. 2012, Considerations for using Spatial Scans with WFC3, Tech. rep.
- Mordasini, C., van Boekel, R., Mollière, P., Henning, T., & Benneke, B. 2016, *ApJ*, 832, 41
- Mountain, C. M., Selby, M. J., Leggett, S. K., Blackwell, D. E., & Petford, A. D. 1985, *A&A*, 151, 399
- Parmentier, V., & Crossfield, I. 2017, *ArXiv e-prints*, arXiv:1711.07696
- Parmentier, V., Fortney, J. J., Showman, A. P., Morley, C., & Marley, M. S. 2016, *ApJ*, 828, 22
- Pont, F., Zucker, S., & Queloz, D. 2006, *MNRAS*, 373, 231
- Sheppard, K. B., Mandell, A. M., Tamburo, P., et al. 2017, *ApJL*, 850, L32
- Showman, A. P., Fortney, J. J., Lian, Y., et al. 2009, *ApJ*, 699, 564
- Southworth, J., Mancini, L., Cicci, S., et al. 2015, *MNRAS*, 447, 711
- Stevenson, K. B., Bean, J. L., Madhusudhan, N., & Harrington, J. 2014a, *ApJ*, 791, 36
- Stevenson, K. B., Harrington, J., Fortney, J. J., et al. 2012, *ApJ*, 754, 136
- Stevenson, K. B., Désert, J.-M., Line, M. R., et al. 2014b, *Science*, 346, 838
- Stevenson, K. B., Line, M. R., Bean, J. L., et al. 2017, *AJ*, 153, 68

- Tinetti, G., Tennyson, J., Griffith, C. A., & Waldmann, I. 2012, *Philosophical Transactions of the Royal Society of London Series A*, 370, 2749
- Van Der Walt, S., Colbert, S. C., & Varoquaux, G. 2011, *Computing in Science & Engineering*, 13, 22
- Wahhaj, Z., Liu, M. C., Biller, B. A., et al. 2011, *ApJ*, 729, 139
- Wöllert, M., & Brandner, W. 2015, *A&A*, 579, A129
- Wong, M. H., Mahaffy, P. R., Atreya, S. K., Niemann, H. B., & Owen, T. C. 2004, *Icarus*, 171, 153
- Zellem, R. T., Swain, M. R., Roudier, G., et al. 2017, *ApJ*, 844, 27
- Zhang, X., & Showman, A. P. 2017, *ApJ*, 836, 73
- Zhou, Y., Apai, D., Lew, B. W. P., & Schneider, G. 2017, *AJ*, 153, 243